Long Pulse FRC Sustainment with Enhanced Edge Driven Rotating Magnetic Field Current Drive

A.L. Hoffman, H.Y. Guo, K.E. Miller, R.D. Milroy

Redmond Plasma Physics Laboratory, University of Washington, Seattle, WA, USA

e-mail contact of main author: hoffman@aa.washington.edu

Abstract: FRCs have been formed and sustained for up to 50 normal flux decay times by Rotating Magnetic Fields (RMF) in the TCS experiment. For these longer pulse times a new phenomenon has been observed: switching to a higher performance mode delineated by shallower RMF penetration, higher ratios of generated poloidal to RMF drive field, and lower overall plasma resistivity. This global data is not explainable by previous RMF theory based on uniform electron rotational velocities or by numerical calculations based on uniform plasma resistivity, but agrees in many respects with new calculations made using strongly varying resistivity profiles. In order to more realistically model RMF driven FRCs with such non-uniform resistivity profiles, a double rigid rotor model has been developed with separate inner and outer electron rotational velocities and resistivities. The results of this modeling suggest that the RMF drive results in very high resistivity in a narrow edge layer, and that the higher performance mode is characterized by a sharp reduction in resistivity over the bulk of the FRC.

1. Introduction

The use of Rotating Magnetic Fields (RMF) to drive toroidal currents and both create and sustain Field Reversed Configurations (FRC) has a long history, primarily in rotamak devices [1]. Most analysis has been based on assuming a uniform plasma resistivity and a uniform electron rotational speed ω_e at some fraction $\zeta = \omega_e/\omega$ of the RMF frequency ω [2,3,4]. For a given RMF amplitude, B_ω, this analysis produces a relationship between applied RMF torque, the plasma resistivity, and the achievable plasma density [5,6]. However, experimentally, when the resistivity was estimated based on the ratio of absorbed RMF power to the square of the driven current, serious discrepancies were noted. Much higher plasma densities and driven currents were produced than calculated, especially when taking into account FRC lengths ℓ_s greater than the RMF antenna length ℓ_a [7]. Under some low ζ drive conditions experimental features were also observed that could not be accounted for by simple uniform resistivity modeling; most notably the RMF not penetrating to the FRC magnetic field null. Although we have always modeled RMF drive in terms of total RMF and resistive torques, assuming that radial plasma flow could redistribute the RMF drive forces, it was difficult to understand how the FRC flux could be maintained with so little RMF drive at the null, where the RMF flow driven *EMF*, $v_r \times B_z$, was unavailable.

The significance of the RMF penetration profile has become more apparent in recent experiments on the TCS (Translation, Confinement, & Sustainment) device [8] where the discharge pulse lengths were extended from 2.5 to 10 msec by increasing the size of the RMF capacitor bank from 30 to 60 kJ. It was then observed that the performance, as indicated by spontaneous switching between different ratios of external confinement field B_e to B_ω, would undergo abrupt changes. This was accompanied by abrupt switches in RMF profile $B_\theta(r)$ between shallower penetration (higher performance) and deeper penetration (lower performance). Recent calculations with non-uniform resistivities, which illuminate the 'edge driven' process [9], provide a mechanism for understanding this phenomenon. The plasma must have high resistivity in the driven, low density edge region, but much lower resistivity throughout the bulk of the FRC. Many features, such as a non-steady behavior with cyclical

RMF tearing and reconnection caused by vastly different edge and central electron rotational speeds, which are predicted by the non-uniform resistivity calculations, are seen in the experimental measurements [9]. A double rigid rotor model with different central and edge resistivities has been developed to analyze experiments, and is used to examine the above performance mode switching.

2. Basic Experimental Operation

TCS has a 2.6-m long, 80-cm internal diameter vacuum chamber, consisting of two 1.25-m long quartz tubes joined by a metal foil lined plastic ring containing vacuum access ports. Various measurements, such as internal magnetic field probing, CO_2 interferometry, and bolometry, are performed through these access ports.

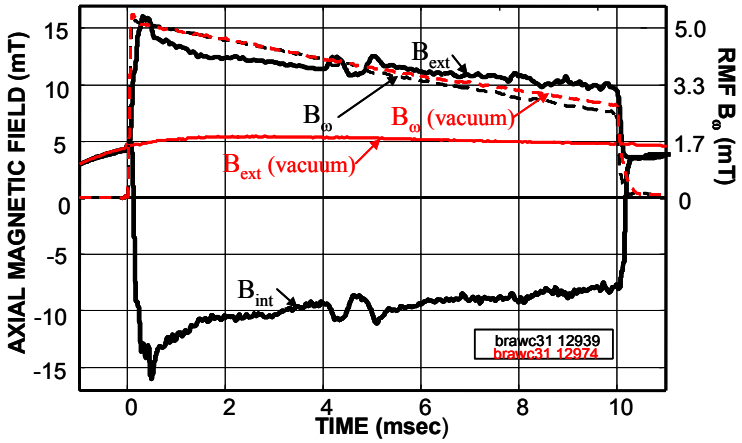

FIG 1. Long pulse operation on TCS.

An axial bias field is provided by a parallel arrangement of 56-turn coils at an effective flux confining radius of 47 cm. The coils are powered by a small capacitor bank with a rise time of about 4 msec, and then crowbarred. There are also copper straps placed directly on the vacuum vessel, with effective L/R field penetration times (in vacuum) of ~4 msec. When the RMF is activated in the presence of a slightly pre-ionized D_2 gas fill and initial axial bias field, an FRC is rapidly formed, compressing the external flux against the flux confining boundaries, and raising the external field. The basic experimental operation is indicated by the time traces of external and internal magnetic fields, and the traces of B_ω (always scaled from the measured RMF antenna currents), shown in Fig. 1. The FRC internal field has approximately the same magnitude as the external field, which is typical of RMF driven FRCs. The operation is very insensitive to the initial puff gas fill pressure (within limits of about a factor of 3). Spectroscopic studies of C and O impurity lines indicate that the density is sustained by recycling after the first half msec, with a magnitude determined by the applied RMF torque and plasma resistivity.

The data shown in this paper were obtained using 1-m long strip antennas, which generally produced deeper penetration profiles than obtained with the original 1.6-m long low inductance tube antennas [7]. The RMF was run at a frequency of 105 kHz. In the discharge shown in Fig. 1 there is an initial startup phase, lasting about one-half msec, where a relatively higher value of B_e is obtained. This peak can be up to 50% higher than during the following period, which is attributed to an initially higher plasma temperature. The temperature is subsequently reduced by recycling impurity ingestion and strong radiation. After startup, the FRC settles into a phase we now call 'lower performance'. However, after about 4 msec B_{ext} and B_{int} begin to vary in an oscillatory manner, and then settle into a 'higher performance' mode after 5-6 msec. This higher performance mode is always accompanied by the generation of a steady toroidal field of about 1-2 mT near the FRC field null (which is usually a precursor to the first jump in B_z). The behavior is highly repeatable, although the exact timing and number of transitions can vary somewhat from shot to shot.

The resistivity inferred from achieved densities and external fields is up to a factor of two lower during the higher performance mode.

B_ω, and the resultant external field and FRC separatrix radius, decrease during the discharge, primarily due to multi-MW losses in the drive tubes of the RMF power supply. There is also some decay due to the 1.5 – 0.5 MW absorbed by the FRC during the pulse, as seen by the differences between the plasma and vacuum traces of B_ω in Fig. 1. After the first half msec, bolometric measurements show that a large fraction of the absorbed power is radiated away, which limits the plasma total temperature to 20-40 eV. The peak plasma density decays from about $2\text{x}10^{19}$ m^{-3} to $1\text{x}10^{19}$ m^{-3} during the discharge, roughly proportional to the decay in B_ω. It is seen however, that the ratio of B_e/B_ω increases, which is an unambiguous indication of higher performance.

3. Analysis

The azimuthal RMF force on the electrons, $\langle j_{ez} B_r \rangle$ is due to the RMF induced in-phase axial oscillation of the electrons interacting with the radial component of the RMF. This translates into an applied torque equal to

$$T_{RMF} = \frac{2\pi r_s \delta^* B_\omega^2}{\mu_o} \ell_a \quad , \qquad (1)$$

where r_s is the FRC separatrix radius and δ* is the RMF penetration distance [3]. Examination of the RMF internal structure in Fig. 2 gives an intuitive idea of why this is so. The RMF magnitude is approximately doubled over its vacuum value B_ω near the FRC separatrix due to the presence of the axial shielding currents j_z, but the forces act in a sine squared manner with respect to azimuthal angle. We analyze current drive in terms of torques since the RMF forces can be transferred to the FRC interior by various mechanisms, and must balance the total resistive retarding torque on the electrons. In the past, analytical expressions have been used for the RMF penetration distance δ* ($\delta^* \sim (2\eta/\mu_o\varpi)^{1/2}$, with $\varpi = \omega - \omega_e$), but these are inappropriate for a plasma with non-uniform resistivity and rotation velocity. We will use actual measured values of δ*, along with Eq. (1), in our data reduction analysis. Numerical calculations show this gives reasonable values for T_{RMF} even with non-uniform resistivity.

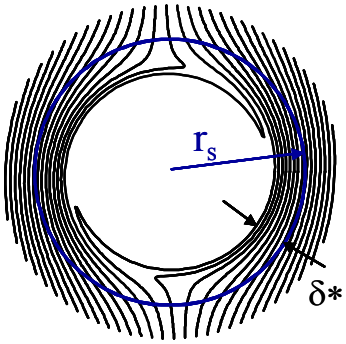

FIG 2. Calculated internal RMF.

As a first step we analyze experimental results for the retarding torque on the electrons based on a simple Rigid Rotor (RR) profile, with $B_z(r) = B_e \tanh K_{RR} u$, $n_e(r) = n_m \text{sech}^2 K_{RR} u$ and $u = (r/R)^2 - 1$ where $R = r_s/\sqrt{2}$ is the location of the field null for an elongated FRC [12]. K_{RR} is a form factor near unity. Assuming a uniform resistivity $\eta_{RR} = m_e \nu_{ei}/e^2 n_e$, the torque on the electrons is then

$$T_{\eta RR} = 0.5\pi e^2 n_m^2 \tanh K_{RR} \left(1 - \tfrac{1}{3}\tanh^2 K_{RR}\right)(\omega_e - \omega_i) r_s^4 \eta_{RR} \ell_s / K_{RR} \quad . \qquad (2)$$

We have included the ion rotation speed $\omega_i = 2\pi f_i$ since RMF driven FRCs are observed to spin up to about $f_i \sim 9$ kHz in the driven electron direction. Calling $\omega_{RR} = \omega_e - \omega_i$, the peak value of external field is $B_e = \mu_o e n_m \omega_{RR} r_s^2 / 4K_{RR}$, and the torque can be expressed in terms of the external magnetic field, which is the most accurately measured quantity.

$$T_{\eta RR} = 2\pi e n_m \tanh K_{RR} \left(1 - \tfrac{1}{3}\tanh^2 K_{RR}\right) r_s^2 \eta_{RR} \ell_s (B_e / \mu_o) \qquad (3)$$

Equating Eqs. (1) and (3) yields a rigid rotor value for the average plasma resistivity.

$$\eta_{RR} = \frac{B_\omega^2(\delta^*/r_s)\ell_a/\ell_s}{en_m \tanh K_{RR}(1-\frac{1}{3}\tanh^2 K_{RR})B_e} = \frac{1020B_\omega^2(\mathrm{mT})(\delta^*/r_s)\ell_a/\ell_s}{n_m(10^{19}\,\mathrm{m}^{-3})B_e(\mathrm{mT})}\ \mu\Omega\cdot\mathrm{m} \qquad (4)$$

where we have taken $K_{RR} = 1$, which is an appropriate fit for the measured profiles. The RR profile has an edge value $B_z(r_s) = B_e \tanh K_{RR}$ and the above analysis does not take into account the resistive torque exerted by the edge plasma, where B_z increases to B_e and $n_e(r)$ drops from $n_m \mathrm{sech}^2 K_{RR}$ to zero.

If we calculate the resistivity based on the measured absorbed power, as has been done in the past [5,6], the ratio of resistivity measured in this way, to that of Eq. (4), is given by $P_{abs}/(\omega_e T_{\eta RR})$ (we use ω_e rather than ω_{RR} for power calculation since the RMF force acts on the electrons). This ratio always considerably exceeds unity, which implies that the resistivity cannot be uniform. The recent numerical calculations of Ref. 9 show that the resistivity must be much higher in the edge region than in the center in order to account for many of the observed data. We have thus developed a double rigid rotor (DRR) model, with an interior rotation speed difference between ions and electrons of ω_{ri}, and an edge rotation $\omega_{re} = \omega - \omega_i$. The ion rotation is assumed uniform, consistent with Doppler broadening measurements [5]. We assume the inner region extends out to a location $u^* < 1$. This value, and the value of ω_{ri}, are determined from requiring the DRR profile to have the same $\langle\beta\rangle$ as measured from internal probes, and making it produce the measured B_e. For a given value of K_i for the inner region, the edge region K_e can be determined by matching n_e and B_z at u^*. The solutions can be obtained from graphical plots of u^* for K_i chosen to best match the actual profile. We use $K_i = 1$, but the final results have very little dependence on this choice. u^* always turns out to be between 0.6 and 0.85, corresponding to r^* between $1.27R$ and $1.36R$, very close to the separatrix at $r_s = 1.41R$. Equilibrium constraints thus result in a very narrow edge region where the density decreases to near zero, in agreement with observations for our RMF driven FRCs. This contrasts with the simple $K_{RR} = 1$ RR value of $n_e(r_s)/n_m = \mathrm{sech}^2 1 = 0.42$.

Calling $F(x) = \tanh x(1 - (\tanh^2 x)/3)$ and η_i and η_e the resistivities in the inner and edge regions respectively, the DRR torque is calculated as

$$T_{\eta DRR} = 0.5\pi e^2 n_m^2 \omega_{ri} r_s^4 (F(K_i u^*)/K_i)\left\{\eta_i + (\omega_{ri}K_e/\omega_{re}K_i)\left(\frac{F(y)}{F(K_i u^*)} - 1\right)\eta_e\right\}\ell_s \ . \qquad (5)$$

K_e is always fairly large (to bring the separatrix density down to near zero, and the parameter $(\omega_{ri}K_e/\omega_{re}K_i)$ is generally about 1.5. The parameter y ($B_z(r_s) = B_e \tanh y$) is also determined from the profile and matching conditions, and is always between 1.5 and 2.5. If we divide the torque into inner and outer contributions, $T_{\eta i}$ and $T_{\eta e}$, the absorbed power is given by

$$P_{abs\theta} = (\omega_{ri} + \omega_i)T_{\eta i} + \omega T_{\eta e} \ . \qquad (6)$$

Equating Eq. (5) to Eq. (1), and Eq. (6) to the measured absorbed power, gives us simultaneous equations for the inner and outer resistivities. We have used $P_{abs\theta}$ to represent the portion of absorbed power attributable to the azimuthal currents, and the largest source of error in the analysis lies in choosing this fraction. We use $P_{abs\theta} = P_{abs}/(1 + (B_\omega/B_e)^2)$, which is fairly arbitrary, but choosing the full measured P_{abs} in Eq. (6) sometimes yields negative values of η_i, and reducing $P_{abs\theta}$ further (by say $1 + (r_s/\delta^*)(B_\omega/B_e)^2$) sometimes gives unrealistic results with η_e less than the average value. In the data reduction we will use these two limits to place error bars on the calculations of η_i.

4. Resistivity Measurements

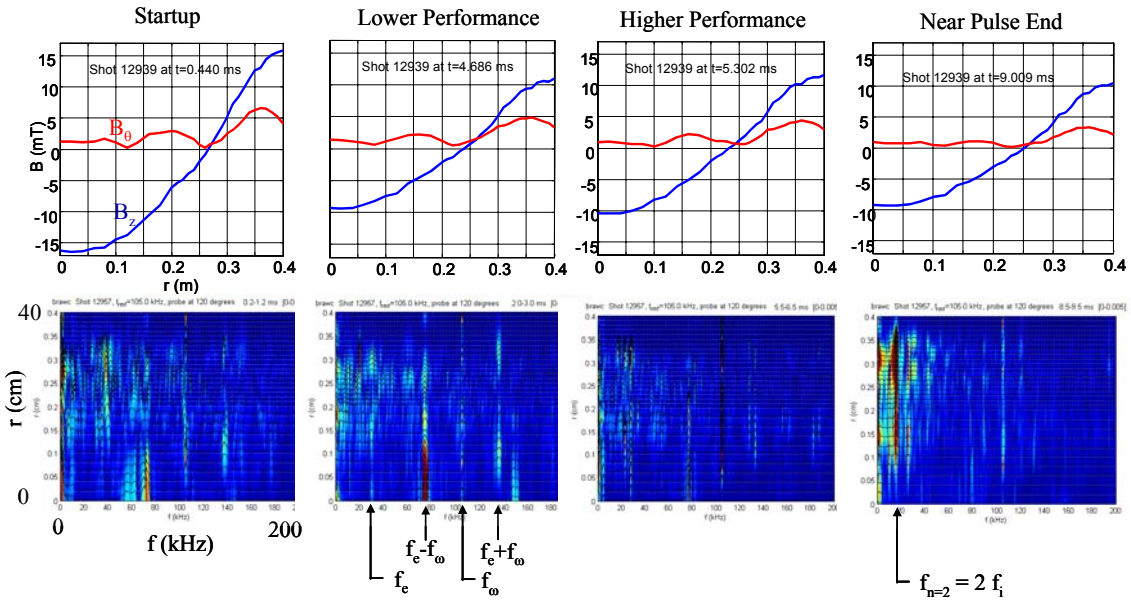

FIG 3. Profile data for discharge 12939 with B_z frequency data for discharge 12957.

The internal magnetic field profiles $B_z(r)$ and $B_\theta(r)$ (assumed to be represented by the measured B_x), are shown in Fig. 3 for four times in a particular discharge. The profiles were obtained with an array of 29 single axis internal probes inserted from the top of TCS and oriented at 45° to the plasma tube centerline so that they were sensitive to both B_z and B_x. The component at the 105 kHz RMF frequency was assumed to be B_θ and the remainder B_z. The frequency content of B_z alone, obtained with the probe oriented in the z direction for a subsequent discharge, is also shown in the figure.

On careful examination there is a subtle but distinct and highly repeatable difference in the B_θ profiles during the lower and higher performance phases. During the lower performance phase B_θ extrapolates smoothly to zero somewhere inside the field null. This is as would be expected from simple, uniform resistivity calculations. Based on 2-dimensional (r,θ) calculations it is not understood why some 105 kHz signal reappears inside the field null, but it is probably due to 3-dimensional effects since axial oscillatory currents on outer field lines should be reflected by similar currents on their inner field line connection. During the higher performance phase, the B_θ profile extrapolates to zero well outside the FRC field null. This is seen to produce a relatively higher value of externally generated field B_e, and the drive performance, as characterized by the ratio of B_e/B_ω continuously improves once the higher performance phase becomes steady, as the RMF magnitude decreases.

The average difference between electron and ion rotation frequencies needed to produce the measured B_e based on the measured density profile is about 35 kHz for all the long pulse data. The calculated DRR central value of $f_{ri} = \omega_{ri}/2\pi$ is about 25 kHz. The contour plots of frequency content show a distinct peak at ~30 kHz, which is seen in the non-uniform resistivity numerical calculations (generally showing up when the outer resistivity is specified to be about ten times the inner resistivity) due to an inner electron rotation at $f_{ri} + f_i$ [9]. In the calculations this frequency is due to some inner RMF rotating at $f_{ri} + f_i$ and

continually tearing and reconnecting with the outer RMF rotating at the full f_ω. The non-steady behavior produces a non-steady torque, which also results in an oscillation in all $B_z(r)$ and B_e. The behavior also produces sidebands about f_ω, which are clearly seen in both B_z and B_θ. The f_{ri} + f_i and sideband oscillations are much more prominent during the low performance phase.

TABLE 1: RESISTIVITIES INFERRED FROM DRR MODEL

Shot	δ^*/r_s	n_m ($10^{19}m^{-3}$)	η_{RR} (μΩ-m)	η_{pabs} (μΩ-m)	η_{inner} (μΩ-m)	η_{outer} (μΩ-m)
12939 0.4 ms	0.16	1.70	109	260	**30**	**235**
4.7 ms	0.21	1.05	209	432	**95**	**393**
5.3 ms	0.185	1.26	124	393	**3**	**357**
9.3 ms	0.195	1.21	97	347	**21**	**347**
12889 6.3 ms	0.23	0.95	269	425	**204**	**291**
7.0 ms	0.18	1.10	136	345	**28**	**394**
12951 4.2 ms	0.21	1.12	212	404	**127**	**333**
5.0 ms	0.18	1.38	114	349	**3**	**351**

Resistivities inferred from the simple RR calculations and from the DRR model for the four times shown in Fig. 3 are listed in Table 1, along with data from lower (red entries) and higher performance modes for two other discharges. The values of δ^*/r_s are taken from the $B_\theta(r)$ traces based on the position where B_θ decreases to one-half its peak value. Since the inferred resistivity is linearly dependent on this value, there is some room for error, but the maximum possible RMF torque given by analytic calculations [3] corresponds to an effective value of δ^*/r_s = 0.38, and the procedure is reasonable. The listed value or η_{RR} is given by Eq. (4). B_ω and B_e are measured accurately, but our cross-tube CO_2 interferometer is only valid for the first 2 msec due to vibrations, and the line density values for later times are scaled from cross-tube continuum radiation measurements. The peak density is calculated from the pressure profile, including contributions from both the ion centrifugal force and the RMF $\langle j_z B_\theta \rangle$ radial force, assuming the total temperature is uniform. This procedure should be reasonably accurate, even after the formation phase, since the density doesn't vary much. It is notable that n_m, along with B_e, increases during the transition from the lower to higher performance mode.

The values of η_{pabs} are given by the RR formula $(P_{abs\theta}/\omega_e T_{RMF})\eta_{RR}$ where ω_e is taken as $\zeta\omega + \omega_i$. ζ is determined from internal probe measurements and the measured line density, and is between 0.29 and 0.35 for all conditions except the 9.3 msec entry, where it is 0.24. It can be seen that η_{pabs} always exceeds η_{RR} by at least a factor of two, which we infer is attributable to a high edge resistivity where most of the RMF power (always over 50%) is absorbed. The greater the difference, the greater will be the calculated difference between η_i and η_e in our DRR modeling. It can be seen that during the higher performance mode η_i is generally under 30 μΩ-m. This value is reasonable given the relatively high ratios v_{De}/v_{ti} of electron drift velocity to ion thermal speed ($v_{De} = \omega_r r \sim 5\times10^4$ m/s near the field null and 2×10^5 m/s near the edge, with $v_{ti} \sim 3\times10^4$ m/s everywhere), which tend to lead to drift wave micro-turbulence. The much higher ratios of v_{De}/v_{ti} in the outer edge, along with any RMF induced turbulence, would be expected to result in much higher resistivities.

The inner and outer resistivities calculated using the DRR model are plotted in Fig. 4 versus the simple RR resistivity η_{RR}. Error bounds are shown on η_i based on the various assumptions mentioned earlier of how much of P_{abs} is assigned to $P_{abs\theta}$. The leftmost

grouping corresponds to the higher performance mode, or to the startup condition for discharge 12939 (orange dashed lines). The blue diamonds are based on assuming $P_{abs\theta} = P_{abs}$, which clearly leads to non-physical negative values of η_i. The upper limit orange triangles are also somewhat non-physical since, in the lower performance cases they sometimes lead to values of η_e being less than η_i. Only the most likely value of edge resistivity is shown.

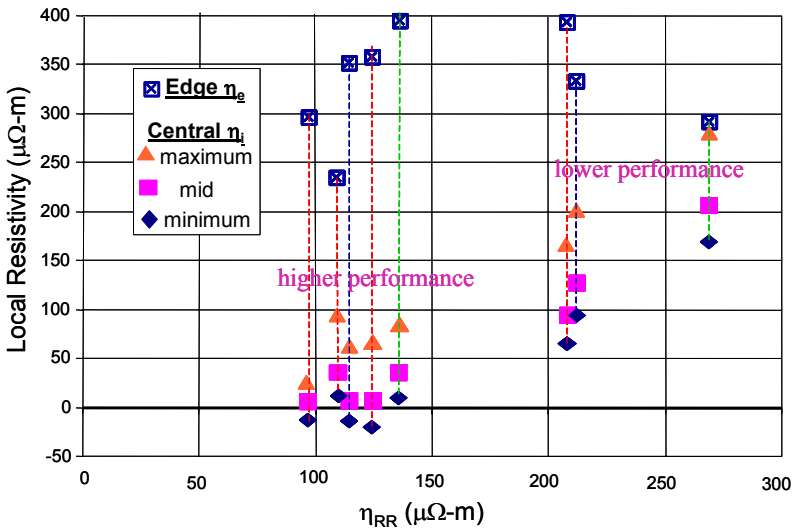

FIG 4. Inner and outer FRC resistivities.

Lower central resistivities during the higher performance phase could be the reason why the RMF penetration is shallower. The lower resistivity would also correlate with the smaller f_{ri} + f_i frequency content seen in the B_z frequency content contour plots in Fig. 3, since less inner torque would be required to maintain the plasma current there. In the latter stages of the discharge a strong component appears at 18 kHz. This is exactly twice the ion rotation frequency, and is due to an n=2 distortion which normally develops for such rapidly rotating FRCs. The radial pressure imposed by B_ω has been measured to have a strong stabilizing effect on the rotating n=2 instability [11], but the ion rotation frequency is almost independent of the magnitude of B_ω. It is thus not surprising that the n=2 distortion develops as the RMF magnitude runs down.

5. Summary and Conclusions

It is possible to both form FRCs and sustain them in quasi steady-state using rotating magnetic fields. A much better understanding of the current drive process has been obtained through the use of detailed profile and frequency spectrum measurements coupled with numerical calculations. The RMF drive process appears to be characterized by strong drive in the edge region near the FRC separatrix, accompanied by fairly high plasma resistivity. The measured interior and edge values are fairly typical of Chodura type resistivity ($\eta \sim (1000/n_e^{1/2}(10^{19}\ m^{1/2}))[1-\exp(v_{De}/fv_{ti})]$ μΩ·m with $f \sim 3$) which was used to model previous FRC flux decay [13].

A higher performance mode appears to develop spontaneously for longer RMF pulse lengths, at least under the circumstances under which the TCS experiments were run. A trigger for this mode has not been identified, but it may be related to the aforementioned appearance of toroidal field. The net result appears to be fairly low interior plasma resistivities. Plasma turbulence is minimized when the RMF magnitude is small compared to the axial confinement field. These conditions were only achievable in TCS at low values of B_ω since the plasma temperature, which along with plasma density sets the diamagnetic current in high

beta FRCs, was held low by impurity radiation. Better performance at higher values of B_ω should be achievable if impurity content can be lowered and temperatures raised.

The edge drive properties of RMF, along with the resultant high edge resistivity and high edge thermal deposition, may rule out RMF as a stand-alone FRC current drive mechanism. However, RMF can be extremely useful for startup, and has been seen to greatly enhance particle lifetimes and interchange stability. It should be ideally suited to be used in conjunction with tangential neutral beam injection (TNBI) current drive near the field null, since the RMF torque, which leads to plasma rotation, could be balanced by TNBI momentum injection in the opposite direction. It may even be possible to influence the azimuthal current and velocity profiles, which could lead to controllable enhancements of performance rather than the spontaneous transitioning between performance modes seen in the pure RMF drive experiments. Monte-Carlo TNBI calculations show that to effectively utilize TNBI the TCS flux levels will have to be raised from present 2 mWb levels (when using the low inductance RMF antennas) to over 5 mWb [14]. This can be done if the plasma temperature can be increased to the 100 eV level. Modifications to minimize impurities are currently underway.

REFERENCES

[1] I.R. Jones, & W.N. Hugrass, "*Steady-state solutions for the penetration of a rotating magnetic field into a plasma colum*n", J. Plasma Physics **26**, 441 (1981).

[2] W.N. Hugrass, "*The influence of the spatial harmonics on the RMF current drive*", Aust. J. Phys. **39**, 513 (1986).

[3] A.L. Hoffman, "*Rotating magnetic field current drive of FRCs subject to equilibrium constraints*", Nuclear Fusion **40**, 1523 (2000).

[4] R.D. Milroy, "*An MHD model of RMF current drive in an FRC*", Phys. Plasmas **7**, 4135 (2000).

[5] H.Y. Guo, et. al., "*Formation and steady-state maintenance of FRCs using RMF current drive*", Phys. Plasmas **9**, 185 (2002).

[6] A.L. Hoffman, H.Y. Guo, R.D. Milroy, and Z.A. Pietrzyk., "*Resistivity scaling of RMF current drive in FRCs*", Nuclear Fusion **43**, 1091 (2003).

[7] H.Y. Guo, A.L. Hoffman, "*Sustainment of elongated FRCs with localized RMF current drive*", Phys. Plasmas **11**, 1087 (2004).

[8] A.L. Hoffman, et. al., "*The TCS Rotating Magnetic Field FRC current-drive experiment*", Fusion Technology **41**, 92 (2002).

[9] R.D. Milroy, K.E. Miller, "*Edge-driven RMF current drive of FRCs*", Phys. Plasmas **11**, 633 (2004).

[10] J.T. Slough, K.E. Miller, "*Enhanced confinement and stability of an FRC with RMF current drive*", Phys. Rev. Lett. **85**, 1444 (2000).

[11] H.Y. Guo, A.L. Hoffman, R.D. Milroy, G.R. Votroubek, "*Stabilization of interchange modes by rotating magnetic fields*", submitted to Phys. Rev. Lett (2004).

[12] M. Tuszewski, "*Field Reversed Configurations*", Nucl. Fusion **28**, 2033 (1988).

[13] R.D. Milroy, J.T. Slough, "*Poloidal flux loss and axial dynamics during the formation of a field-reversed configuration*", Phys. Fluids **30**, 3566 (1987).

[14] A.F. Lifschitz, R. Farengo, A.L. Hoffman, "*Calculations of TNBI current drive efficiency for present moderate flux FRCs*", Nuclear Fusion **44**, 1015 (2004).